Electrostatically defined quantum dots in a Si/SiGe heterostructure

2010 New J. Phys. 12 113019

(http://iopscience.iop.org/1367-2630/12/11/113019)

New Journal of Physics
The open-access journal for physics

Electrostatically defined quantum dots in a Si/SiGe heterostructure

A Wild[1], J Sailer[1], J Nützel[1], G Abstreiter[1], S Ludwig[3,4] and D Bougeard[1,2,4]

[1] Walter Schottky Institut, Technische Universität München, Am Coulombwall 4, 85748 Garching, Germany
[2] Institut für Experimentelle und Angewandte Physik, Universität Regensburg, 93040 Regensburg, Germany
[3] Fakultät für Physik and Center for NanoScience, Ludwig-Maximilians-Universität München, Geschwister-Scholl-Platz 1, 80539 München, Germany
E-mail: bougeard@wsi.tum.de and ludwig@lmu.de

New Journal of Physics **12** (2010) 113019 (16pp)
Received 13 July 2010
Published 10 November 2010
Online at http://www.njp.org/
doi:10.1088/1367-2630/12/11/113019

Abstract. We present an electrostatically defined few-electron double quantum dot (QD) realized in a molecular beam epitaxially grown Si/SiGe heterostructure. Transport and charge spectroscopy with an additional QD as well as pulsed-gate measurements are demonstrated. We discuss technological challenges specific to silicon-based heterostructures and the effect of a comparably large effective electron mass on transport properties and tunability of the double QD. Charge noise, which might be intrinsically induced due to strain engineering, is proven not to affect the stable operation of our device as a spin qubit.

[4] Authors to whom any correspondence should be addressed.

Contents

1. Introduction

Electrostatically defined quantum dot (QD) structures are attracting increasing interest as building blocks for solid-state-based quantum information processing. In such structures, the electron spin decoherence time is crucial for coherent manipulation of spin qubits. Electron spin phenomena have already been investigated in QD structures in AlGaAs/GaAs heterostructures [1]. The hyperfine interaction of the electrons confined in such QDs with roughly 10^5 fluctuating nuclear spins has been identified as a limiting decoherence mechanism for electron spin qubits in GaAs [2]–[4]. This problem can be addressed by manipulating nuclear spins in GaAs [5]–[7] or by choosing an alternative host material. Silicon (Si) as a host material offers a promising path towards extending the electron spin coherence time compared to GaAs-based qubits, because naturally composed Si crystals contain only a fraction of about 4.7% of the nuclear spin-carrying isotopes [8], compared to 100% in GaAs. Since the hyperfine interaction strength is roughly proportional to the fraction of nuclear spin-carrying isotopes, much longer coherence times are expected for Si. Furthermore, Si has a weaker spin–orbit interaction [9, 10] and is not piezo-electric [11].

Recently, promising efforts towards the implementation of spin qubits in natural Si have been made in three classes of devices: electrostatically defined QDs in strain-engineered Si/SiGe heterostructures [12]–[16], QDs in metal-oxide-semiconductor (MOS) structures [17]–[21] or MOS–phosphorus hybrid devices [22]–[26]. In some of these devices, the first pulsed-gate experiments on Si-based QDs have been performed, including spin relaxation time measurements (T_1) of a confined electron [15, 21, 26], the demonstration of single-shot readout [26] and the measurement of tunneling rates [16, 23].

In this emerging research field, open questions remain, such as the influence of Si/SiGe-specific material properties on device performance and tunabillity. In this paper, we present a Si/SiGe heterostructure whose material properties can be precisely controlled in molecular beam epitaxy (MBE). The heterostructure contains a strain-induced high-mobility two-dimensional electron system (2DES) and is equipped with metallic top-gates. In the resulting device, we implement a double QD combined with a single-electron transistor (SET) as a charge sensor, both tunable by the field effect. An important fundamental difference of Si- to GaAs-based structures is the considerably larger effective electron mass in the 2DES ($m^*_{\mathrm{e,Si}} = 0.19 \times m_\mathrm{e} \approx 3 \times m^*_{\mathrm{e,GaAs}}$). We discuss the direct consequences of a high electron mass, which can be observed e.g. in the form of a small Fermi energy of the 2DES and low tunneling rates of electrons across

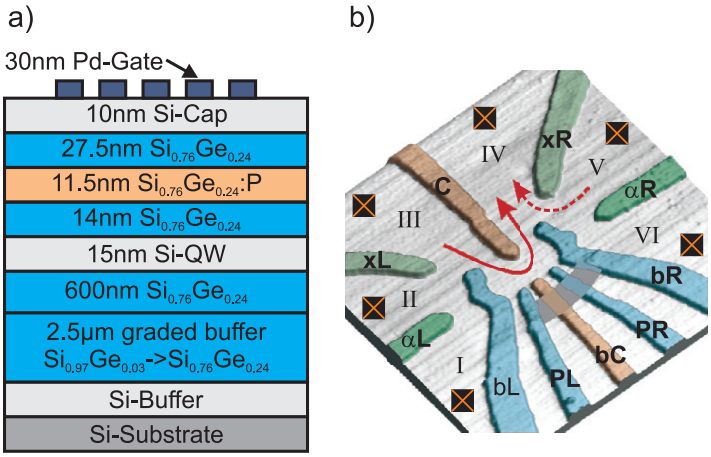

Figure 1. (a) Layout of the MBE Si/SiGe heterostructure showing the layer structure. Evaporated palladium gates deplete parts of the 2D electron gas in the silicon quantum well (Si-QW). (b) AFM micrograph of the gates defining the double QD. Due to a short circuit symbolized by a bold stripe, gates PL, bC, PR and bR are on an identical potential. The occupation of the double QD is tuned via gate voltages V_{bL} and V_{bR}. In a direct transport spectroscopy experiment, current flows between contacts III and IV (solid arrow). In addition, a single QD, defined by gate bR and xR, can be used as a charge sensor. In this case, current flows between the contacts V and IV (dashed arrow).

electrostatic barriers. In our measurements, charge noise strongly affects a large-scale stability diagram, but is a minor issue as long as gate voltages are changed only slightly. Thereby, we demonstrate stable operation of our double QD device and its suitability as a spin qubit.

2. Material and sample development

Our double QD is electrostatically formed within a 2DES in a strained-Si quantum well (QW) of an MBE grown $\mathrm{Si}/\mathrm{Si}_{1-x}\mathrm{Ge}_x$ heterostructure with $x = 24\%$. The layout and composition of the heterostructure are shown in figure 1(a). A layer doped by phosphorus gives rise to a maximum 2DES density of about $3.5 \times 10^{11}\,\mathrm{cm}^{-2}$ and an electron mobility of $1.1 \times 10^5\,\mathrm{cm}^2\,(\mathrm{Vs})^{-1}$ in this wafer at the temperature $T = 1.4\,\mathrm{K}$. The biaxial tensile strain in the Si QW lifts the sixfold valley degeneracy of bulk Si. The energy of the two valleys in the [0 0 1] growth direction is lowered by 230 meV below the conduction band edge of the surrounding $\mathrm{Si}_{0.76}\mathrm{Ge}_{0.24}$ layers. From a 1D self-consistent band structure calculation with nextnano++ [27, 28], we obtain an intravalley subband spacing between the first two subbands of the order of 8 meV, which is large compared to the Fermi energy of $E_{\mathrm{F}} = 1.1\,\mathrm{meV}$. This small Fermi energy, compared to typical GaAs heterostructures, is a consequence of the high effective electron mass in Si and the twofold valley degeneracy.

The double QD is defined in a mesa fabricated by wet chemical etching. Ohmic contacts are formed by diffusing Sb/Au into the heterostructure. Electric top-gates are fabricated by electron beam lithography and palladium (Pd) evaporation [29]. The Pd on the device surface pins the Fermi energy at about 750 meV [30, 31] below the conduction band edge. This strong pinning

is a consequence of surface states at the Pd–Si interface. The surface states bind most of the electrons otherwise remaining at the doping layer. Together with the high work function of Pd, this results in a large Schottky barrier. The latter helps to minimize leakage currents from biased gates into the heterostructure. Our double QD gate design has been adapted from comparable GaAs-based structures [32]. A nominally identical device to the one investigated in this work is shown in an AFM micrograph in figure 1(b). High-frequency coaxial cables lead to the gates bL and bR on the sample surface, while all other gates are connected via low-frequency wires. After cooldown to $T_{2DES} \approx 100\,\mathrm{mK}$, samples from the studied wafer require weak illumination with a red LED in order to populate the 2DES. We find that even at zero applied bias, the mere presence of Pd on top of the Si cap layer completely depletes the 2DES underneath. This behavior has been observed before [33]–[35] and is mainly a consequence of the saturation of Si dangling bonds [36] and the related Fermi level pinning at the Pd–Si interface [37] at low doping concentrations. Consequently, positive voltages are typically applied to all gates in order to drive currents from ohmic contacts III or V to IV. An unintended electrical short between gates PL, bC, PR and bR forces these gates to be on the same electrical potential. We will refer to this potential as V_{bR} in the following. As a consequence of the short, the inter-dot barrier, the energy levels and the tunnel barriers from both dots to the leads cannot be tuned independently.

3. Results and discussion

3.1. Transport spectroscopy

Figure 2 depicts the dc current I_{DQD} flowing across the serial double QD as a function of the gate voltages V_{bL} and V_{bR}. I_{DQD} is measured at contact IV, while a dc bias of $V_{SD} = -750\,\mu\mathrm{V}$ is applied to contact III. The charge stability diagram shows the typical honeycomb pattern reminiscent of a double QD. $I_{DQD} > 0$ is observed on the triple points, but also along charging lines. I_{DQD} completely disappears below $V_{bR} \leqslant 205\,\mathrm{mV}$ and towards the lower left corner of the stability diagram. On the triple points, the charge fluctuates on both QDs and linear response transport by sequential tunneling is expected. However, in contrast to our observation, no current is expected along the charging lines as one of the QDs is in Coulomb blockade. In this regime, the observed non-zero I_{DQD} along charging lines is maintained by elastic and inelastic co-tunneling and enhanced by the comparatively large V_{SD}.

The widths $\delta V_L^{bL,bR}$ and $\delta V_R^{bL,bR}$ of the charging lines in figure 2 with respect to the gate voltage axis V_{bL} and V_{bR} serve as a calibration scale to convert the applied gate voltage into energy. We find the lever arms $\alpha_L^{bL} = eV_{SD}/\delta V_L^{bL} \approx 0.18\mathrm{e}$, $\alpha_R^{bR} = eV_{SD}/\delta V_R^{bR} \approx 0.39\mathrm{e}$, $\alpha_L^{bR} = eV_{SD}/\delta V_L^{bR} \approx 0.31\mathrm{e}$ and $\alpha_R^{bL} = eV_{SD}/\delta V_R^{bL} \approx 0.07\mathrm{e}$. The lever arms are then used to deduce typical charging energies of both QDs from the distances ΔV_L and ΔV_R between parallel charging lines in figure 2. The charging energies are of the order of $E_{CL} = \alpha_L^{bL} \cdot \Delta V_L \leqslant 1.5\,\mathrm{meV}$ and $E_{CR} = \alpha_R^{bR} \cdot \Delta V_R \leqslant 1.6\,\mathrm{meV}$. Based on a 3D self-consistent band structure calculation performed with nextnano++, where we take into account the dot capacitances for the given gate geometry, we estimate the double QD occupation of about $N_L \approx N_R \approx 18$ electrons[5].

The disappearance of I_{DQD} below $V_{bR} \leqslant 205\,\mathrm{mV}$ and the overall large effective resistance $V_{SD}/I_{DQD} \geqslant 60\,\mathrm{M\Omega}$ for the stability diagram are in part caused by the large effective electron mass m^* in Si-based 2DES since tunneling rates are exponentially suppressed as the mass

[5] A simple disc model for the double QD based on the 2DES density and charging energies typically overestimates the occupation by a factor of 2 compared to the self-consistent band structure simulation.

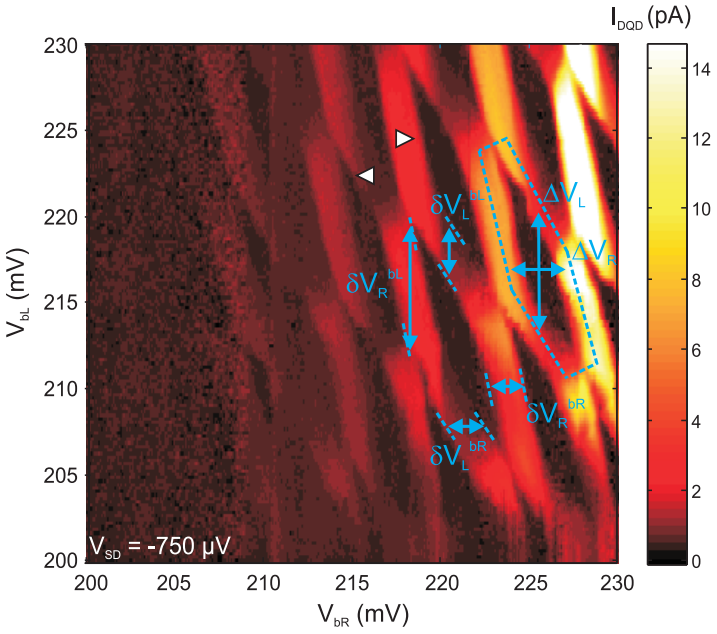

Figure 2. Charge stability diagram that shows the dc current I_{DQD} as a function of V_{bL} and V_{bR} flowing through the double QD, while a bias of $-750\,\mu$V is applied at contact III. The width of the charging lines $\delta V_{\mathrm{L}}^{\mathrm{bL,bR}}$ and $\delta V_{\mathrm{R}}^{\mathrm{bL,bR}}$ correspond to an energy window (transport window) of $eV_{\mathrm{SD}} = 750\,\mu$eV defined by the applied bias. They define the lever arms $\alpha_{\mathrm{L}}^{\mathrm{bL}} \approx 0.18$e, $\alpha_{\mathrm{R}}^{\mathrm{bR}} \approx 0.39$e, $\alpha_{\mathrm{L}}^{\mathrm{bR}} \approx 0.31$e and $\alpha_{\mathrm{R}}^{\mathrm{bL}} \approx 0.07$e and allow a conversion of the voltages V_{bL} and V_{bR} into energy. The distances between consecutive charging lines ΔV_{L} and ΔV_{R} can be converted into the charging energies $E_{\mathrm{CL}} \approx 1.5$ meV and $E_{\mathrm{CR}} \approx 1.6$ meV of the QDs.

of the tunneling particle is increased. However, in our device, the low I_{DQD} is furthermore a consequence of the short between gates PL, bC, PR and bR. This short not only results in a strong capacitive coupling of V_{bR} to the right, but also to the left QD and in a strong suppressing effect of V_{bR} on the QD-lead tunneling rates. Furthermore, V_{bR} can be expected to asymmetrically influence the tunneling rates of the left and right QDs to its leads. We can observe the effect of asymmetric QD-lead tunneling rates in figure 2 in a larger current value along the charging lines of the right QD (marked by $\triangleright$ in figure 2) compared to the charging lines of the left QD (marked by $\triangleleft$ in figure 2). Away from the triple points, current along the charging lines of the right (left) QD involves a first-order tunneling process and a second-order co-tunneling process in series. The current is roughly given by

$$I_{\mathrm{DQD}}^{\triangleright} \propto \frac{\Gamma_{\mathrm{L}}\Gamma_{\mathrm{iD}}\Gamma_{\mathrm{R}}}{\Gamma_{\mathrm{L}}\Gamma_{\mathrm{iD}} + \Gamma_{\mathrm{R}}\Delta/\hbar} \qquad \text{and} \qquad I_{\mathrm{DQD}}^{\triangleleft} \propto \frac{\Gamma_{\mathrm{L}}\Gamma_{\mathrm{iD}}\Gamma_{\mathrm{R}}}{\Gamma_{\mathrm{R}}\Gamma_{\mathrm{iD}} + \Gamma_{\mathrm{L}}\Delta/\hbar}. \tag{1}$$

Here, Γ_{L} and Γ_{R} are the respective QD-lead tunneling rates and Γ_{iD} is the inter-dot tunneling rate. The asymmetry energy Δ separates the energies of the localized states with the electron being either in the left or in the right QD. As we observe $I_{\mathrm{DQD}}^{\triangleright} > I_{\mathrm{DQD}}^{\triangleleft}$ (where we use the realistic assumption $\Delta < \hbar\Gamma_{\mathrm{iD}}$), which corresponds to $\Gamma_{\mathrm{R}} < \Gamma_{\mathrm{L}}$, the tunnel coupling between the right QD and its lead is weaker than the tunneling coupling between the left QD and its lead.

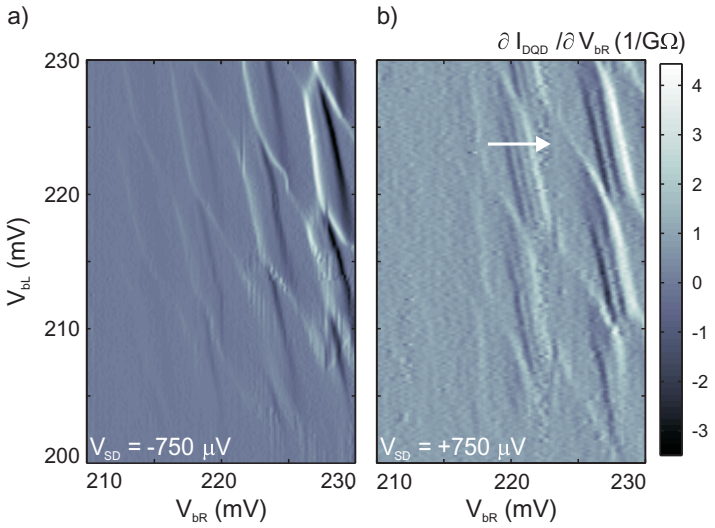

Figure 3. Transconductance $\partial I_{\mathrm{DQD}}/\partial V_{\mathrm{bR}}$ of the double QD as a function of V_{bL} and V_{bR} for an applied bias of $-750\,\mu$V (a) and $+750\,\mu$V (b). Charging lines of the left QD are barely visible, whereas charging lines of the right QD exhibit an additional substructure only for $+750\,\mu$V. This substructure is not present for $-750\,\mu$V.

Figure 3 contrasts the transconductance $\partial I_{\mathrm{DQD}}/\partial V_{\mathrm{bR}}$ for an applied dc bias of $-750\,\mu$V, as in figure 2, with the corresponding measurement for an applied bias of $+750\,\mu$V. Due to $\Gamma_{\mathrm{R}} < \Gamma_{\mathrm{L}}$, and in agreement with the current measurement in figure 2, the charging lines of the right QD are more pronounced compared to those of the left QD. For positive V_{SD}, a substructure within the charging line of the right QD of width $eV_{\mathrm{SD}}/\alpha_{\mathrm{R}}^{\mathrm{bR}}$ is visible in the form of parallel lines of alternating high and low transconductance. No such lines are observable for negative V_{SD}.

This situation is discussed in figure 4 in more detail. Figure 4(a) plots $I_{\mathrm{DQD}}(V_{\mathrm{bR}})$ as well as the corresponding transconductance $\partial I_{\mathrm{DQD}}/\partial V_{\mathrm{bR}}\,(V_{\mathrm{bR}})$ for $V_{\mathrm{SD}} = +750\,\mu$V along the horizontal white arrow in figure 3(b). $|I_{\mathrm{DQD}}|$ increases in steps as V_{bR} is increased, while the transconductance shows corresponding oscillations. These observations are explained in figure 4(b) by explicitly taking resonant tunneling and co-tunneling processes into account. Electrons can tunnel resonantly from the right lead IV into the right QD followed by an elastic co-tunneling process via the Coulomb-blocked left QD into the left lead III. Note that inelastic co-tunneling processes are also possible, but do not change our qualitative argument. Dotted lines in figure 4(b) mark the single-particle excitation spectrum of the right QD. The observed current steps and transconductance oscillations in figure 4(a) for $V_{\mathrm{SD}} > 0$ imply that the excited states of the right QD contribute separately to I_{DQD} as depicted by arrows in figure 4(b). This also implies that the energy relaxation rate Γ_{E} within the right QD is slow compared to the co-tunneling rates between the right QD and the left lead III. In figure 4(a), we resolve two excited states with a characteristic excitation energy of approximately $200\,\mu$eV. For $V_{\mathrm{SD}} < 0$, no excited states are observed along the charging lines of the right QD in figure 3(a). Here a co-tunneling process is followed by resonant tunneling from the right QD to the right lead IV as sketched in figure 4(c). However, energy relaxation in the right QD is fast compared to the slow tunneling rate Γ_{R}. Hence, the missing excitation spectrum of the right QD for $V_{\mathrm{SD}} < 0$ not only confirms the previous finding $\Gamma_{\mathrm{R}} < \Gamma_{\mathrm{L}}$, but also suggests $\Gamma_{\mathrm{R}} \ll \Gamma_{\mathrm{L}}, \Gamma_{\mathrm{iD}}$.

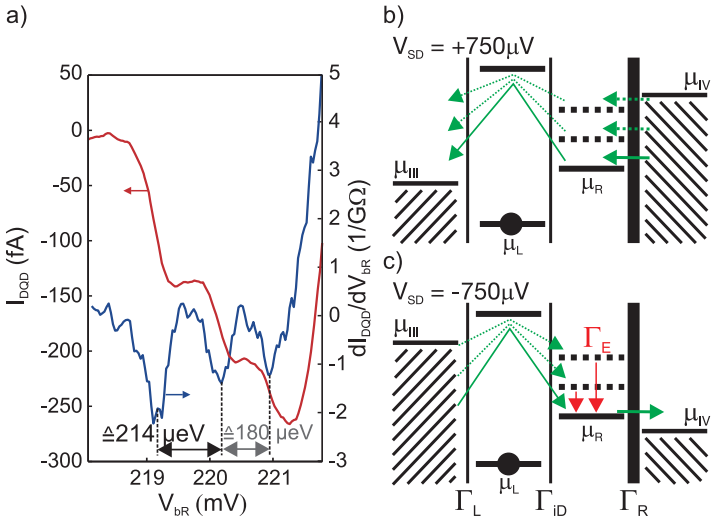

Figure 4. (a) Cross section along the white arrow in figure 3(b). The double QD current I_{DQD} is shown on the left axis and its derivative, the transconductance $\partial I_{\mathrm{DQD}}/\partial V_{\mathrm{bR}}$, is shown on the right axis. Energy level configuration and likely transport channels (arrows) are shown for $V_{\mathrm{SD}} = +750\,\mu\mathrm{V}$ in (b) and $V_{\mathrm{SD}} = -750\,\mu\mathrm{V}$ in (c). Transport in the double QD takes place by resonant tunneling through the right QD and co-tunneling through the Coulomb-blocked left QD.

3.2. Charge sensing

In an attempt to characterize the double QD in the few-electron regime, we use charge sensing [32] via a QD SET. The QD is located between gates bR, α_{R} and xR. Current is measured from contact V to IV as illustrated by the dashed arrow in figure 1(b). The Coulomb-blockade oscillations of the sensor QD are plotted in the inset of figure 5(a) for a sensor bias of $V_{\mathrm{SD}} = 400\,\mu\mathrm{eV}$. Its charging energy is approximately $E_{\mathrm{C}} \approx 1.5\,\mathrm{meV}$. As the working range of the charge sensor, we choose one of the flanks of a Coulomb peak where $|\partial I_{\mathrm{Sensor}}/\partial V_{\mathrm{xR}}|$ and thus the sensor sensitivity have local maxima. The main plot of figure 5(a) shows $\Delta I_{\mathrm{Sensor}} = I_{\mathrm{Sensor}} - \gamma V_{\mathrm{bL}}$, which is the sensor current after subtraction of a straight line (γV_{bL}). It represents the direct capacitive coupling between the sensor QD and gate bL as a function of V_{bL}. The pronounced steps mark single-electron charging events of the double QD. The transconductance $\partial(\Delta I_{\mathrm{Sensor}})/\partial V_{\mathrm{bL}}$ plotted in figure 5(b) exhibits sharp local maxima where I_{Sensor} has steps. The charge sensor has a resolution of at least 0.1 electron charge determined from its signal-to-noise ratio. More importantly, it allows us to measure the charge stability diagram in a regime where a current through the double QD is already too small to be detected by standard techniques. This is especially important in order to control the few-electron regime in Si-based serially coupled QDs where the large effective mass of the electrons causes weak tunnel couplings.

From the step heights in $\Delta I_{\mathrm{Sensor}}$ and the peak shape in $\partial I_{\mathrm{Sensor}}/\partial V_{\mathrm{bL}}$, we can distinguish charging events of the left (L) or right (R) QD, a nearby charge trap (F) or inter-dot (iD) transitions. Since the capacitive coupling between the right QD and the sensor is stronger, the associated steps are higher (R) compared to steps associated with charging events of the left QD

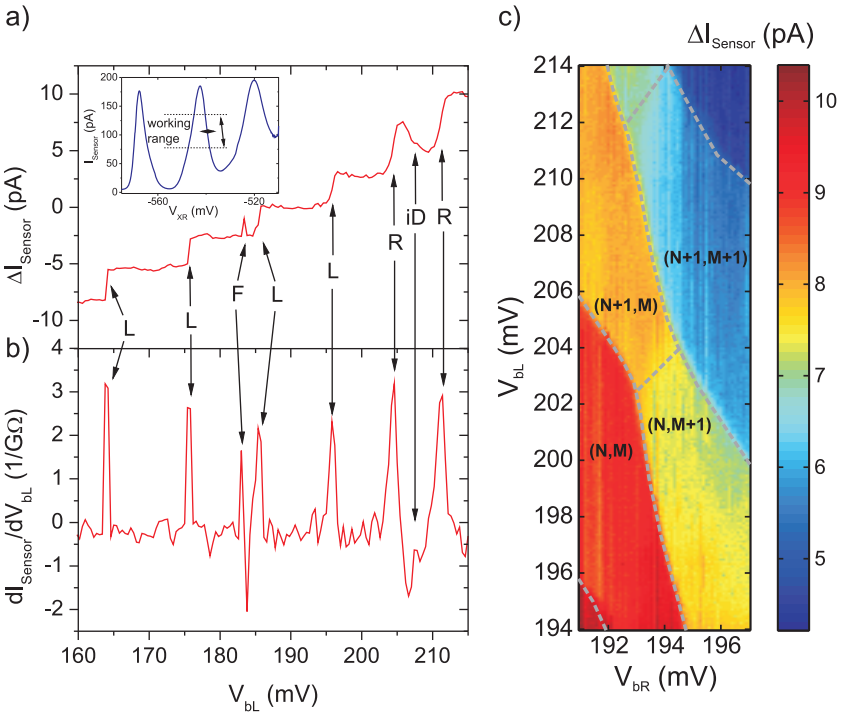

Figure 5. A QD SET as a charge sensor: (a) the inset plots $I_{\mathrm{Sensor}}(V_{\mathrm{xR}})$, showing Coulomb blockade oscillations. A dedicated working range is marked. The main plot shows the sensor current after subtraction of a linear background $\Delta I_{\mathrm{Sensor}} = I_{\mathrm{Sensor}} - \gamma V_{\mathrm{bL}}$ for $V_{\mathrm{bR}} = 200\,\mathrm{mV}$. (b) Numerical derivative $\partial(\Delta I_{\mathrm{Sensor}})/\partial V_{\mathrm{bL}}$. (c) Charge stability diagram in the vicinity of two triple points that shows $\Delta I_{\mathrm{Sensor}}$ as a function of V_{bL} and V_{bR} for different stable ground state charge configurations (different colors).

(L). An inter-dot transition (iD) where an electron moves from the right to the left QD results in a decrease of $\Delta I_{\mathrm{Sensor}}$ and thus in a transconductance minimum. In addition, a nearby charge fluctuation causes a local maximum of $\Delta I_{\mathrm{Sensor}}$ (F).

During long measurements over a wide plunger gate voltage range, cross-talk and charge fluctuations in the environment can cause a considerable drift of the sensor working point out of its working range, which we define by horizontal lines in the inset of figure 5(a). In order to avoid such a drift of the sensor, gate xR is used for stabilization of the local potential of the charge sensor. We perform a linear adjustment of $V_{\mathrm{xR}}(V_{\mathrm{bL}})$ during each plunger gate sweep and a stepwise adjustment after each V_{bR} step. This technique has been used for the charge stability diagram in figure 5(c). It plots the sensor current as a function of V_{bL} and V_{bR} from which a plane fit has been subtracted. Regions of stable ground state charge configurations are marked by $(N, M) \leftrightarrow (N+1, M+1)$ for N, $N+1$ electrons in the left QD and M, $M+1$ electrons in the right QD.

Figure 6 shows the transconductance $\partial I_{\mathrm{Sensor}}/\partial V_{\mathrm{bL}}$ for a larger gate voltage regime compared to figure 5(c). Charging lines are white ($\partial I_{\mathrm{Sensor}}/\partial V_{\mathrm{bL}} > 0$), whereas reconfiguration lines are black ($\partial I_{\mathrm{Sensor}}/\partial V_{\mathrm{bL}} < 0$). This large-scale stability diagram was obtained by sweeping V_{bL} from 220 to 150 mV and stepping V_{bR} from high to low voltages. The plot contains

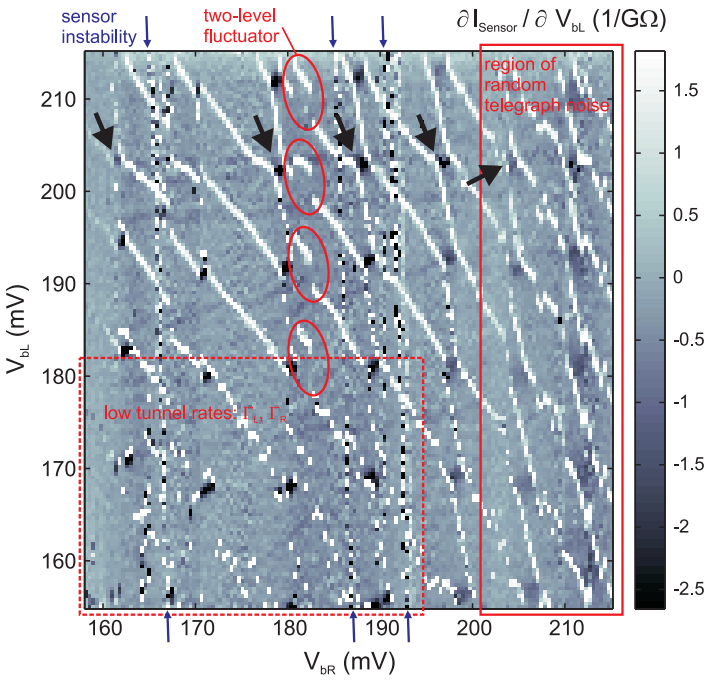

Figure 6. Large-scale charge stability diagram showing the sensor transconductance $\partial I_{\mathrm{Sensor}}/\partial V_{\mathrm{bL}}$. Stable regimes alternate with noisy areas. Charge noise, which mainly affects the sensor QD, is marked by blue arrows. A specific fluctuator that causes a bistability is marked by red ellipses and a region of overall strong charge noise that directly affects the double QD is framed by a red box. The lower left corner (dashed box) features very low QD-lead tunneling rates Γ_{L} and Γ_{R}.

stable regions, but is riddled with noisy areas. Most of the observed noise can be attributed to fluctuating charges in the vicinity of the nanostructure (charge noise). For $V_{\mathrm{bR}} > 200\,\mathrm{mV}$, local potential fluctuations at the double QD are present and result in random telegraph noise. In contrast, for $V_{\mathrm{bR}} < 200\,\mathrm{mV}$ the local potential of the double QD is relatively stable. The red ellipses at $V_{\mathrm{bR}} \approx 182\,\mathrm{mV}$ mark a bistability caused by a specific two-level charge fluctuator with a characteristic time constant of several minutes. Fluctuations running almost vertically through the diagram are marked by blue arrows at the top and bottom of the plot. They do hardly affect the charging lines, but primarily the background signal at stable double QD charge configurations. They can be attributed to local potential fluctuations restricted to the sensor QD.

The stability diagram of figure 6 shows the general tendency that the appearance of fluctuations strongly depends on V_{bR}, while V_{bL} has almost no influence. This can be interpreted as a hint that the observed telegraph noise is not a general problem of the heterostructure, but is rather linked to the unintended short between the gates PL, bC, PR and bR, all lying on the same potential. Lateral leakage currents along the sample surface are likely to cause the short. These leakage currents can also trigger charge fluctuations, which result in the observed telegraph noise.

In addition, the risk of vertical leakage currents is higher for strain-engineered Si/SiGe heterostructures compared to AlGaAs/GaAs-based structures. The plastic strain relaxation

process during SiGe epitaxy leads to the formation of threading dislocations (TD) [38, 39], which can pierce all the way from the graded buffer SiGe layer (see figure 1(a)) through the strained Si-QW to the surface. These crystal defects in Si/SiGe heterostructures are associated with mid-band gap states along the TD. The latter are a possible source of charge fluctuations [40, 41] at the surface. Furthermore, the presence of TDs could facilitate vertical leakage currents from a biased gate into the heterostructure. However, in the case of figure 6, such leakage currents are too small to be directly observed. Transmission electron microscopy and atomic force microscopy measurements of our heterostructures suggest TD densities typically lower than $10^7\,\mathrm{cm}^{-2}$. This corresponds to a less than 5% probability of finding even a single TD in the direct vicinity of the double QD or the sensor QD. Hence, TDs are expected to play only a minor role in the charge noise observed in figure 6.

In general, our charge sensing experiments demonstrate an important tendency. Despite locally strong charge noise for voltage sweeps covering a large range as in figure 6, stable operation of the double QD, as well as the sensor, is possible in small gate voltage intervals. Irrespective of the exact origin of occasional charge noise, this local stability is more essential and should allow the successful realization and stable operation of qubits.

We now turn to the lower left part of figure 6, encircled with a dashed box. Here, the number of electrons charging each QD is well below 10. Below $V_{\mathrm{bL}} = 180\,\mathrm{mV}$ and for decreasing values of V_{bR}, first, charging lines associated with the right QD, and then, those associated with the left QD, become discontinuous or even vanish. In contrast to the previous discussion, this phenomenon is not caused by charge noise, but results from decreasing tunnel couplings between the QDs and their leads as the plunger gate voltages are decremented [16, 42]. More accurate measurements of the dc sensor current I_{Sensor} in such a regime are shown in figure 7(a). The data were taken by sweeping V_{bL} at a rate of $0.5\,\mathrm{mV\,s}^{-1}$ (vertical sweeps from the top to the bottom of section (i) take $t_{\mathrm{sweep}} = 20\,\mathrm{s}$) and by stepping V_{bR} from the right to the left in between vertical sweeps. The data were measured subsequently for the three intervals (i), (ii) and (iii). Here, we plot the numerical derivative $\partial I_{\mathrm{Sensor}}/\partial V_{\mathrm{bL}}$. This transconductance shows no charging lines associated with the right QD. Hence, for the applied gate voltages, the right QD is effectively decoupled from the leads. The typical resonant charge fluctuation time of the right QD is longer than the time taken by a vertical sweep. In section (i), charging lines for the left QD and reconfiguration lines are still visible. Thus resonant charge exchanges via the left and the inter-dot barrier are fast compared to the duration of a vertical sweep. In section (ii), charging lines are more and more interrupted as V_{bR} is decreased. At the same time, the reconfiguration lines become elongated. This trend continues in section (iii) at even more negative V_{bL} where the charging lines are absent but the reconfiguration lines are vastly extended towards lower V_{bR}.

Whereas in figure 7(a) resonant charge fluctuations in the right QD are generally suppressed, between sections (i) and (iii), we clearly observe a transition to the situation in which charging events in both QDs become much slower than the vertical sweep time of about $t_{\mathrm{sweep}} = 20\,\mathrm{s}$. The elongated and clearly visible charge reconfiguration lines show that charge exchange between the two QDs is still fast compared to the sweep time. Hence in section (iii) of figure 7(a), the double QD tends to occupy a non-equilibrium charge configuration because of $\Gamma_{\mathrm{L}}, \Gamma_{\mathrm{R}} \ll t_{\mathrm{sweep}}^{-1}$, whereas the charge distribution between the two QDs still tends to minimize the overall energy because of $\Gamma_{\mathrm{iD}} \gg t_{\mathrm{sweep}}$. From the length of the reconfiguration lines, we estimate for instance $\Gamma_{\mathrm{L}} \approx 0.1\,\mathrm{Hz}$ at $V_{\mathrm{bL}} = 155\,\mathrm{mV}$ and $V_{\mathrm{bR}} = 175\,\mathrm{mV}$, whereas $\Gamma_{\mathrm{L}} \gg 1\,\mathrm{Hz}$ if V_{bL} is increased by only about 20 mV.

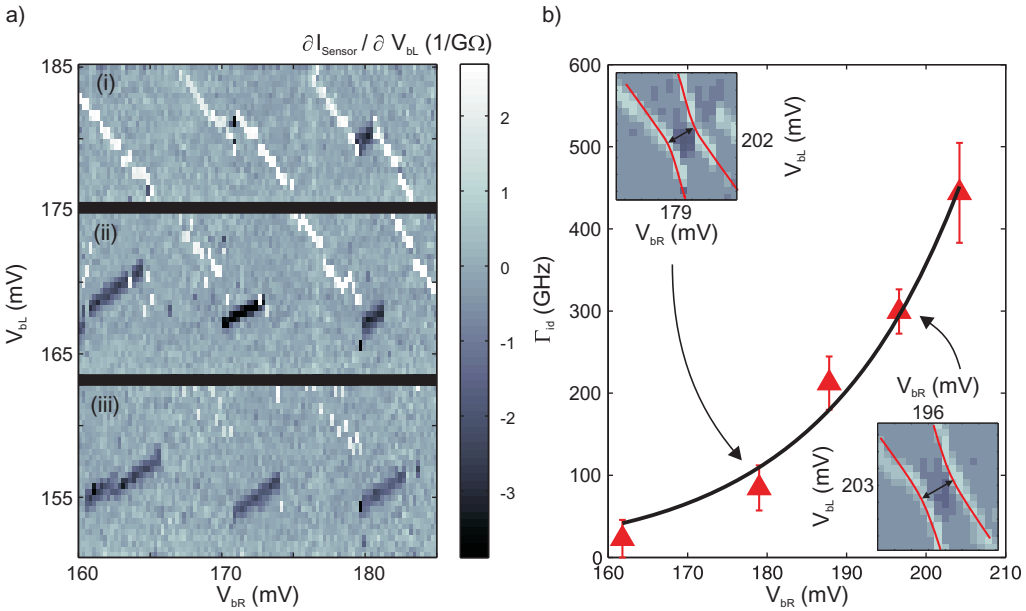

Figure 7. (a) Charge stability diagram in the lower left isolation regime of figure 6. The diagram is composed of three sections (i), (ii) and (iii) that have been measured successively. The tunneling rates change from $\Gamma \gg 1\,\mathrm{Hz}$ to $\Gamma \ll 1\,\mathrm{Hz}$ in the depicted regime, giving rise to discontinuous or absent charging lines. (b) Inter-dot tunneling rate $\Gamma_{\mathrm{iD}}(V_{\mathrm{bR}})$. Triangles are obtained by fitting avoided crossings near triple points marked by black arrows in figure 6. Insets show exemplary avoided crossings in the stability diagram. The solid line in the main plot is a Wentzel–Kramers–Brillouin (WKB) fit.

This measurement features two tendencies: tunneling rates are strongly susceptible to changes in gate voltage and tunneling rates are generally low. Both tendencies can be partly attributed to the large effective electron mass m_{e}^* in Si-based 2DES, since in first order, the tunneling rate across a barrier is proportional to $\exp(-\sqrt{m_{\mathrm{e}}^* \cdot E_{\mathrm{B}}})$, where the height of the tunnel barrier E_{B} is proportional to the applied gate voltages.

The dependence of the inter-dot tunneling rate Γ_{iD} on the applied gate voltage V_{bR} is more quantitatively investigated in figure 7(b). The data points are obtained by fitting the charging lines at the avoided crossings near the triple points marked by black arrows in figure 6 for almost constant $V_{\mathrm{bL}} \approx 203\,\mathrm{mV}$. Exemplarily, two of the fits are shown as insets in figure 7(b). The distance between the solid lines is described by the function $\Delta E = \sqrt{(2\Delta)^2 + (\hbar\Gamma_{\mathrm{iD}})^2} + E_{\mathrm{C}}$ where $2\Delta = (\mu_{\mathrm{R}} - \mu_{\mathrm{L}})$ is the asymmetry energy of the quantum-mechanical two-level system and E_{C} is the classical charging energy that represents the electrostatic coupling between the two QDs [43, 44]. In order to fit the charging lines in a stability diagram based on applied gate voltages, in addition a linear transformation via the lever arms α_i^j (compare 3.1) and a rotation of the coordinate system is employed [44]. Assuming E_{C} to be constant within a small range of applied gate voltages, we find best fits for $E_{\mathrm{C}} \approx 435\,\mu\mathrm{eV}$ and the tunneling rates Γ_{iD} in figure 7(b). The solid line in figure 7(b) is a fit curve based on the WKB approximation for the inter-dot tunnel coupling $\Gamma_{\mathrm{iD}} = \Gamma_0 \cdot \exp(-d\sqrt{m_{\mathrm{e}}^* E_{\mathrm{B}}}/\hbar) \sim \exp(\beta V_{\mathrm{bR}})$, where we assume for simplicity a constant width d of the tunnel barrier and the barrier height $E_{\mathrm{B}} = E_{\mathrm{B}}^0 - \alpha_{\mathrm{B}} V_{\mathrm{bR}}$ and

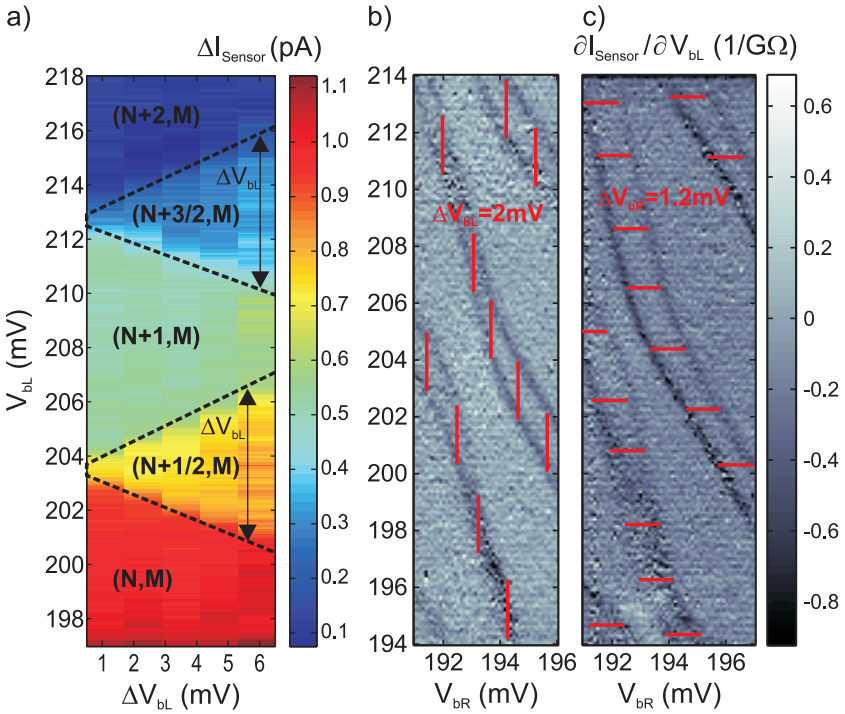

Figure 8. (a) Charge sensor current $\Delta I_{\mathrm{Sensor}}(V_{\mathrm{bL}})$ when a rectangular pulse sequence with 50% duty cycle modulates V_{bL} by ΔV_{bL}. In between charge plateaus with integer occupation, intermediate plateaus emerge with increasing ΔV_{bL}. (b, c) Transconductance $\Delta\partial I_{\mathrm{Sensor}}/\partial V_{\mathrm{bL}}$ while pulsing with a 50% duty cycle for the charge stability diagram shown in figure 5(c). Pulses are applied to gate bL (b) or bR (c). Red lines mark the pulse amplitude.

use $\alpha_{\mathrm{B}} V_{\mathrm{bR}}/E_{\mathrm{B}}^{0} \ll 1$. The gate-barrier lever arm is defined by $\alpha_{\mathrm{B}} = E_{\mathrm{B}}/V_{\mathrm{bR}}$. Then the scaling factor β depends on m_{e}^{*}, d and α_{B}. From the fitting procedure we find $\beta = 0.056 \pm 0.023\,\mathrm{mV}^{-1}$, which corresponds to $\Delta V_{\mathrm{bR}} \approx 40\,\mathrm{mV}$ that are required to change the tunneling rate by one order of magnitude. This value is rather small compared to similar experiments with GaAs-based double QDs [45, 46]. The observed strong dependence of the tunneling rate on the gate voltage can in part be attributed to the higher effective electron mass in Si.

The tendency for small tunneling rates that strongly depend on gate voltages has been independently observed for QD-lead tunneling in figure 7(a) and inter-dot tunneling in figure 7(b). It has the following two direct implications: due to the small tunneling rates, transport spectroscopy in the few-electron regime is more difficult in Si compared to double QDs defined in GaAs because of much smaller currents. In contrast, the strong dependence of the tunneling rates on gate voltage is a chance for experiments that require time-dependent tunnel barriers—as is often the case in quantum information processing.

3.3. Pulsed-gate experiments

Spin-based quantum information processing requires fast initialization and manipulation of the spins in a double QD. We have combined charge sensing with pulsed gate operation [47] to demonstrate, as a first step, switching between two charge configurations.

Figure 8(a) shows the dc-charge sensor current $\Delta I_{\mathrm{Sensor}}(V_{\mathrm{bL}})$ for a fixed voltage V_{bR}, while a rectangular pulse sequence of amplitude ΔV_{bL} with a 50% duty cycle and a period of 1 ms modulates V_{bL}. With increasing pulse amplitude, two triangular-shaped intermediate plateaus with average charge configurations $(N+1/2, M)$ and $(N+3/2, M)$ develop. The vertical extension of the intermediate plateau is identical to ΔV_{bL}. This result demonstrates the effect of a sudden change in a gate voltage, namely a shift of the local potential that defines the double QD. This local potential difference results in a shift of the entire stability diagram for the duration of the pulse. For the applied pulse train with a 50% duty cycle, we therefore expect to find two copies of the stability diagram shifted according to the pulse direction and amplitude. This can be seen in figures 8(b) and (c) where the pulses were applied to gate bL (b) and bR (c) with amplitudes of $\Delta V_{\mathrm{bL}} = 2\,\mathrm{mV}$ and $\Delta V_{\mathrm{bR}} = 1.2\,\mathrm{mV}$, respectively. Clearly, the charging lines split into doublets of parallel charging lines with the corresponding distance ΔV_{bL} or ΔV_{bR} as recently demonstrated also for other Si-based devices [16, 23]. Due to the strong inter-dot coupling, the reconfiguration lines are rather broadened than split.

The low QD-lead tunneling rates Γ_{L} and Γ_{R} in the few-electron regime restrict our pulse repetition rates to no more than about 10 kHz before charge transitions of the QD cannot follow the pulse sequence instantaneously anymore, similar to [16]. We have also performed pulse repetition rates up to approximately 5 MHz limited by our instruments in the regime of larger QD-lead tunneling rates.

4. Conclusion

In summary, we have performed direct transport spectroscopy through a few-electron Si/SiGe double QDs, charge-sensing with a remote single QD sensor and pulsed-gate measurements. We deduce material-specific implications for the implementation of double QDs and spin qubits. An important parameter influencing the transport properties of our QD devices is the comparatively large effective electron mass m_{e}^{*} in Si-based 2DES. It enhances the dependence of tunneling rates on gate voltage and correspondingly can cause overall low tunneling rates across electrostatic barriers. Additionally, the large m_{e}^{*} contributes to a small Fermi energy, together with the twofold valley degeneracy. The combination of low tunneling rates and small Fermi energies hampers linear response transport spectroscopy with a current flowing across double QDs in the few-electron regime. However, these difficulties can be circumvented by smaller feature sizes in future devices. From another perspective, the relatively strong scaling of tunneling rates with gate voltage can be exploited to implement efficient tuning of tunneling rates by pulsing gate voltages with a limited amplitude. As an alternative to transport spectroscopy, a spin qubit can also be operated at a constant overall charge of a double QD in combination with charge spectroscopy. Based on such measurements, we find QDs in our Si/SiGe heterostructure devices still exposed to more charge noise than mature GaAs-based devices. Yet, our experiments also demonstrate a promising tendency towards quiet operation of the double QD when manipulating gate voltages only in a limited range. These results suggest a realistic path towards Si-based quantum information processing.

The key advantage of Si-based qubits is the reduced interaction of confined electron spins in Si with their volatile crystal environment that gives rise to a number of decoherence mechanisms. Phonon-mediated back-action of a remote charge sensor on a qubit, which has been observed in GaAs-based QDs [48, 49], can be expected to be much weaker in Si. Indeed, the electron–phonon coupling is reduced (e.g. no piezo-electricity) and the low Fermi energy

reduces the band width for phonon-mediated interaction [48]. Furthermore, the spin–orbit coupling is weak and the hyperfine interaction in natural Si crystals is reduced compared to GaAs. Most importantly, our results show that the presented device layout with the possibility of almost zero Overhauser field in recently realized isotopically purified ^{28}Si 2DES [29] makes Si-based QDs a promising candidate for spin qubits with coherence times much larger than those that can be realized in GaAs/AlGaAs heterostructures.

Acknowledgments

Financial support from the Deutsche Forschungsgemeinschaft via SFB 631 and the 'Nano Initiative Munich (NIM)' is gratefully acknowledged. We thank Daniela Taubert, Daniel Harbusch and Stephan Manus for helpful discussions.

References

[1] Hanson R, Kouwenhoven L, Petta J, Tarucha S and Vandersypen L 2007 Spins in few-electron quantum dots *Rev. Mod. Phys.* **79** 1217
[2] Merkulov I, Efros A and Rosen M 2002 Electron spin relaxation by nuclei in semiconductor quantum dots *Phys. Rev.* B **65** 205309
[3] Witzel W and Das Sarma S 2006 Quantum theory for electron spin decoherence induced by nuclear spin dynamics in semiconductor quantum computer architectures: spectral diffusion of localized electron spins in the nuclear solid-state environment *Phys. Rev.* B **74** 035322
[4] Coish W, Fischer J and Loss D 2008 Exponential decay in a spin bath *Phys. Rev.* B **77** 125329
[5] Petta J, Taylor J, Johnson A, Yacoby A, Lukin M, Marcus C, Hanson M and Gossard A 2008 Dynamic nuclear polarization with single electron spins *Phys. Rev. Lett.* **100** 067601
[6] Vink I T, Nowack K C, Koppens F H L, Danon J, Nazarov Y V and Vandersypen L M K 2009 Locking electron spins into magnetic resonance by electron nuclear feedback *Nature Phys.* **5** 764
[7] Foletti S, Bluhm H, Mahalu D, Umansky V and Yacoby A 2009 Universal quantum control of two-electron spin quantum bits using dynamic nuclear polarization *Nature Phys.* **5** 903
[8] Ager J W and Haller E E 2006 Isotopically engineered semiconductors: from the bulk to nanostructures *Phys. Status Solidi* a **203** 3550
[9] Tahan C and Joynt R 2005 Rashba spin–orbit coupling and spin relaxation in silicon quantum wells *Phys. Rev.* B **71** 075315
[10] Prada M, Blick R H and Joynt R 2010 Spin relaxation in isotopically purified silicon quantum dots *Physica* E **42** 639
[11] Prada M, Blick R H and Joynt R 2008 Singlet-triplet relaxation in two-electron silicon quantum dots *Phys. Rev.* B **77** 115438
[12] Simmons C B, Thalakulam M, Shaji N, Klein L J, Qin H, Blick R H, Savage D E, Lagally M G, Coppersmith S N and Eriksson M A 2007 Single-electron quantum dot in Si/SiGe with integrated charge sensing *Appl. Phys. Lett.* **91** 213103
[13] Shaji N *et al* 2008 Spin blockade and lifetime-enhanced transport in a few-electron Si/SiGe double quantum dot *Nature Phys.* **4** 540
[14] Simmons C B *et al* 2009 Charge sensing and controllable tunnel coupling in a Si/SiGe double quantum dot *Nano Lett.* **9** 3234
[15] Hayes R R *et al* 2009 Lifetime measurements (T1) of electron spins in Si/SiGe quantum dots arXiv:0908.0173
[16] Thalakulam M, Simmons C B, Rosemeyer B M, Savage D E, Lagally M G, Friesen M, Coppersmith S N and Eriksson M A 2010 Fast tunnel rates in Si/SiGe one-electron single and double quantum dots *Appl. Phys. Lett.* **96** 183104

[17] Liu H, Fujisawa T, Inokawa H, Ono Y, Fujiwara A and Hirayama Y 2008 A gate-defined silicon quantum dot molecule *Appl. Phys. Lett.* **92** 222104
[18] Lim W H, Hübl H, Willems van Beveren L, Rubanov S, Spizzirri P G, Angus S J, Clark R G and Dzurak A S 2009 Electrostatically defined few-electron double quantum dot in silicon *Appl. Phys. Lett.* **94** 173502
[19] Nordberg E P *et al* 2009 Charge sensing in enhancement mode double-top-gated metal-oxide-semiconductor quantum dots *Appl. Phys. Lett.* **95** 202102
[20] Hu B and Yang C 2009 Electron spin blockade and singlet-triplet transition in a silicon single electron transistor *Phys. Rev.* B **80** 075310
[21] Xiao M, House M G and Jiang H W 2010 Measurement of the spin relaxation time of single electrons in a silicon metal-oxide-semiconductor-based quantum dot *Phys. Rev. Lett.* **104** 096801
[22] Prati E, Latempa R and Fanciulli M 2009 Microwave-assisted transport in a single-donor silicon quantum dot *Phys. Rev.* B **80** 165331
[23] Hübl H, Nugroho C D, Morello A, Escott C C, Eriksson M A, Yang C, Jamieson D N, Clark R G and Dzurak A S 2010 Electron tunnel rates in a donor-silicon single electron transistor hybrid *Phys. Rev.* B **81** 235318
[24] Morello A, Escott C, Hübl H, Willems Van Beveren L, Hollenberg L, Jamieson D, Dzurak A and Clark R 2009 Architecture for high-sensitivity single-shot readout and control of the electron spin of individual donors in silicon *Phys. Rev.* B **80** 081307
[25] Tan K Y *et al* 2010 Transport spectroscopy of single phosphorus donors in a silicon nanoscale transistor *Nano Lett.* **10** 11
[26] Morello A *et al* 2010 Single-shot readout of an electron spin in silicon *Nature* **467** 687
[27] Trellakis A, Zibold T, Andlauer T, Birner S, Smith R K, Morschl R and Vogl P 2006 The 3D nanometer device project nextnano: Concepts, methods, results *J. Comput. Electron.* **5** 285
[28] Birner S, Zibold T, Andlauer T, Kubis T, Sabathil M, Trellakis A and Vogl P 2007 nextnano: general purpose 3-D simulations *IEEE Trans. Electron Devices* **54** 2137
[29] Sailer J *et al* 2009 A Schottky top-gated two-dimensional electron system in a nuclear spin free Si/SiGe heterostructure *Phys. Status Solidi (RRL)* **3** 61
[30] Kircher C J 1971 Metallurgical properties and electrical characteristics of palladium silicide–silicon contacts *Solid State Electron.* **14** 507
[31] Tongson L L, Knox B E, Sullivan T E and Fonash S J 1979 Comparative study of chemical and polarization characteristics of Pd/Si and Pd/SiOx/Si Schottky-barrier-type devices *J. Appl. Phys.* **50** 1535
[32] Elzerman J, Hanson R, Greidanus J, Willems Van Beveren L, De Franceschi S, Vandersypen L, Tarucha S and Kouwenhoven L 2003 Few-electron quantum dot circuit with integrated charge read out *Phys. Rev.* B **67** 161308
[33] Holzmann M, Többen D, Abstreiter G and Schäffler F 1994 Field-effect induced electron channels in a Si/Si0.7Ge0.3 heterostructure *J. Appl. Phys.* **76** 3917
[34] Többen D, Wharam D, Abstreiter G, Kotthaus J and Schäffler F 1995 Transport properties of a Si/SiGe quantum point contact in the presence of impurities *Phys. Rev.* B **52** 4704
[35] Többen D, Wharam D A, Abstreiter G, Kotthaus J P and Schäffler F 1995 Ballistic electron transport through a quantum point contact defined in a $Si/Si_{0.7}Ge_{0.3}$ heterostructure *Semicond. Sci. Technol.* **10** 711
[36] Tao M, Agarwal S, Udeshi D, Basit N, Maldonado E and Kirk W P 2003 Low Schottky barriers on n-type silicon (001) *Appl. Phys. Lett.* **83** 2593
[37] Schäffler F 1997 High-mobility Si and Ge structures *Semicond. Sci. Technol.* **12** 1515
[38] Beanland R, Dunstan D J and Goodhew P J 1996 Plastic relaxation and relaxed buffer layers for semiconductor epitaxy *Adv. Phys.* **45** 87
[39] Mooney P M 1996 Strain relaxation and dislocations in SiGe/Si structures *Mater. Sci. Eng.* **17** 105
[40] Mooney P M and Chu J O 2000 Si Ge technology: heteroepitaxy and high-speed microelectronics *Annu. Rev. Mater. Sci.* **30** 335
[41] Berbezier I, Ronda A and Portavoce A 2002 SiGe nanostructures: new insights into growth processes *J. Phys.: Condens. Matter* **14** 8283

[42] Rushforth A, Smith C, Godfrey M, Beere H, Ritchie D and Pepper M 2004 Noninvasive detection of the evolution of the charge states of a double dot system *Phys. Rev.* B **69** 113309
[43] van der Wiel W, De Franceschi S, Elzerman J, Fujisawa T, Tarucha S and Kouwenhoven L 2002 Electron transport through double quantum dots *Rev. Mod. Phys.* **75** 1
[44] Hüttel A, Ludwig S, Lorenz H, Eberl K and Kotthaus J 2005 Direct control of the tunnel splitting in a one-electron double quantum dot *Phys. Rev.* B **72** 081310
[45] Petta J, Johnson A, Marcus C, Hanson M and Gossard A 2004 Manipulation of a single charge in a double quantum dot *Phys. Rev. Lett.* **93** 186802
[46] DiCarlo L, Lynch H, Johnson A, Childress L, Crockett K, Marcus C, Hanson M and Gossard A 2004 Differential charge sensing and charge delocalization in a tunable double quantum dot *Phys. Rev. Lett.* **92** 226801
[47] Petta J, Johnson A, Yacoby A, Marcus C, Hanson M and Gossard A 2005 Pulsed-gate measurements of the singlet–triplet relaxation time in a two-electron double quantum dot *Phys. Rev.* B **72** 161301
[48] Schinner G J, Tranitz H P, Wegscheider W, Kotthaus J P and Ludwig S 2009 Phonon-mediated nonequilibrium interaction between nanoscale devices *Phys. Rev. Lett.* **102** 186801
[49] Harbusch D, Taubert D, Tranitz H P, Wegscheider W and Ludwig S 2010 Phonon-mediated versus coulombic backaction in quantum dot circuits *Phys. Rev. Lett.* **104** 196801